Journal of Colloid and Interface Science 454 (2015) 226–237

Contents lists available at ScienceDirect

Journal of Colloid and Interface Science

www.elsevier.com/locate/jcis

Feature Article

# Measurement of surface and interfacial tension using pendant drop tensiometry

Joseph D. Berry [a,b,1], Michael J. Neeson [c,1], Raymond R. Dagastine [b,d], Derek Y.C. Chan [c,e], Rico F. Tabor [f,*]

[a] Commonwealth Scientific and Industrial Research Organisation (CSIRO) Mineral Resources Flagship, Clayton 3169, Australia
[b] Department of Chemical and Biomolecular Engineering, University of Melbourne, Parkville 3010, Australia
[c] School of Mathematics and Statistics, University of Melbourne, Parkville 3010, Australia
[d] Melbourne Centre for Nanofabrication, 151 Wellington Road, Clayton 3168, Australia
[e] Department of Chemistry and Biotechnology, Swinburne University of Technology, Hawthorn 3122, Australia
[f] School of Chemistry, Monash University, Clayton 3800, Australia

## GRAPHICAL ABSTRACT

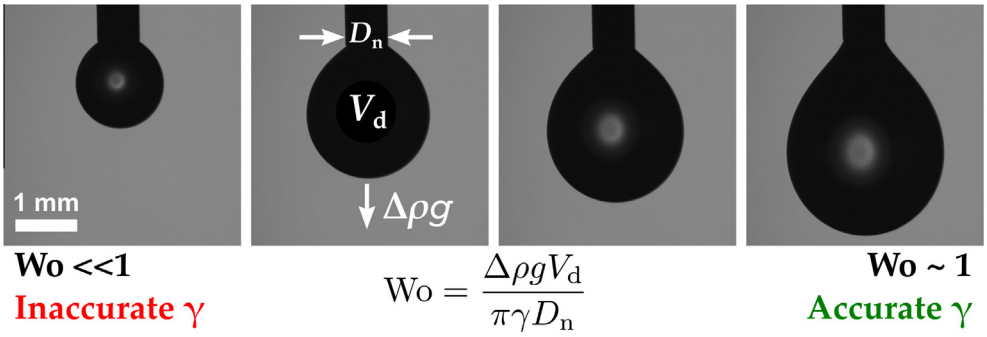


## ARTICLE INFO

*Article history:*
Received 17 April 2015
Accepted 7 May 2015
Available online 15 May 2015

*Keywords:*
Pendant drop
Drop shape analysis
Tensiometry
Surface tension
Interfacial tension
Bond number

## ABSTRACT

Pendant drop tensiometry offers a simple and elegant solution to determining surface and interfacial tension – a central parameter in many colloidal systems including emulsions, foams and wetting phenomena. The technique involves the acquisition of a silhouette of an axisymmetric fluid droplet, and iterative fitting of the Young–Laplace equation that balances gravitational deformation of the drop with the restorative interfacial tension. Since the advent of high-quality digital cameras and desktop computers, this process has been automated with high speed and precision. However, despite its beguiling simplicity, there are complications and limitations that accompany pendant drop tensiometry connected with both Bond number (the balance between interfacial tension and gravitational forces) and drop volume. Here, we discuss the process involved with going from a captured experimental image to a fitted interfacial tension value, highlighting pertinent features and limitations along the way. We introduce a new parameter, the Worthington number, Wo, to characterise the measurement precision. A fully functional, open-source acquisition and fitting software is provided to enable the reader to test and develop the technique further.



*Abbreviations:* IFT, interfacial tension; Bo, Bond number; Wo, Worthington number; LMF–AO, Levenberg–Marquardt–Fletcher – automated optimisation; CMC, critical micelle concentration; CTAB, cetyltrimethylammonium bromide; SDS, sodium dodecylsulfate; RSD, relative standard deviation.

* Corresponding author. Fax: +61 3 9905 4597.
*E-mail address:* Rico.Tabor@monash.edu (R.F. Tabor).

[1] These authors contributed equally to this work.

http://dx.doi.org/10.1016/j.jcis.2015.05.012
0021-9797/

**Contents**



## 1. Introduction

Interfacial tension is a phenomenon that, at the molecular level, results from the difference in energy between molecules at a fluid interface when compared to their bulk counterparts. It is equally correctly described as a measure of how much energy is required to make a unit area of interface between two immiscible liquids, thus taking units of Joules per square metre – equivalent to the more commonly used Newtons per metre. Interfacial tension is a concept of fundamental importance in colloid science, describing phenomena as diverse as the formation, shape and stability of liquid drops [1,2], the surface energy cost in forming an emulsion and the force applied by a capillary liquid bridge. Determination of the interfacial tension allows deductions to be made regarding the chemical composition of fluid interfaces and the adsorption and desorption of surface active solutes. Further, interfacial tension is the dominant force in microfluidic flows that are increasingly used in advanced liquid handling. It follows directly that precise measurement of interfacial tension is of critical importance to both science and industry. Many techniques have been proposed to measure interfacial tension (Fig. 1), and their features and qualities are described in detail by Drelich et al. [3]. Arguably the simplest (in terms of instrumentation), most robust, and most versatile of these methods is pendant drop tensiometry, where the measurement consists simply of a fluid droplet suspended from a needle.[2]

The ability to determine the interfacial tension from the shape of a pendant liquid drop deformed by gravity was first proposed over a century ago by Worthington [4–6], who evaluated the pressure drop across a portion of the curved interface of a drop hanging from a ground glass tube. In 1883, Bashforth and Adams [7] formed comprehensive numerical tables of approximate solutions to the axisymmetric Young–Laplace equation, and these are still in use today. Using an appropriate scaling, they showed that the shape of an axisymmetric pendant drop depended on a single dimensionless quantity, which they termed $\beta$, defined as $\beta \equiv \Delta\rho g R_0^2/\gamma$, where the symbols represent density difference $\Delta\rho$, gravitational acceleration $g$, drop dimension $R_0$ and interfacial tension $\gamma$. Bashforth and Adams [7] described $\beta$ as an "abstract number", when in fact it has significant physical meaning as a measure of the relative importance of gravitational forces to interfacial forces. This quantity was later termed the 'Bond number'[3] by Merrington and Richardson [9] in 1947, named after the British physicist Wilfrid Bond (1897–1937) who introduced the quantity in relation to the terminal velocity of drops and bubbles in 1928 [10].

If one can accurately quantify the Bond number from the drop shape, the interfacial tension readily follows from the known quantities of density, gravity and drop size. However, determining the Bond number for a given system proved difficult. In the 1940s, Andreas et al. [11] devised a simple approach for determining this quantity by taking the ratio of two easily measured experimental quantities: the maximum drop diameter $d_e$, and the drop diameter $d_s$ measured at a distance $d_e$ from the apex. The ratio $S = d_s/d_e$ could then be compared to tables to determine the Bond number, thereby obtaining the interfacial tension. Andreas et al. calculated these tables experimentally, however these were later improved through numerical integration of the Young–Laplace equation [12,13].

This approach offered a simple method for calculating the interfacial tension; however a large portion of data relating to the actual drop profile was discarded. In 1983, two transformational articles were published that developed computational routines to utilise all the available data, which greatly increased the precision of the method [14,15]. These methods compared the entire drop profile to the theoretical drop profile by considering the sum of the squared residuals between each experimental data point and the theoretical drop profile. While the methods share many similarities, the approach of Huh and Reed [15] implements an approximate expression compared to the exact expression presented in

[2] We use 'droplet' throughout for simplicity, although the technique can be equally applied to study gas bubbles in surrounding liquids, and the droplet may be pendant or sessile with respect to the needle, provided that the sign of the density difference is adjusted accordingly. Any combination of immiscible fluids and orientations can be handled theoretically, although some systems may be experimentally challenging to realise.

[3] The Bond number is also known in the literature as the Eötvös number, named after the Hungarian physicist Lóránd Eötvös (1848–1919), who invented the reflection method for the measurement of surface tension and also discovered the linear relationship between the surface tension of a liquid and its temperature (known as the Eötvös law). Eötvös spent the first part of his career studying the effects of capillarity, and then moved on to make important observations on gravity. It is not evident that the Bond number appears in any of the publications of Eötvös. Indeed, it appears to have been named after Eötvös by Harmathy [8] in 1960 firstly to pay homage to a fellow Hungarian, and secondly as a subtle reference to the trajectory of Eötvös' research career. Interestingly, and completely irrelevantly, after coining the Eötvös number Harmarthy went on to invent a one-handed toilet paper dispenser.

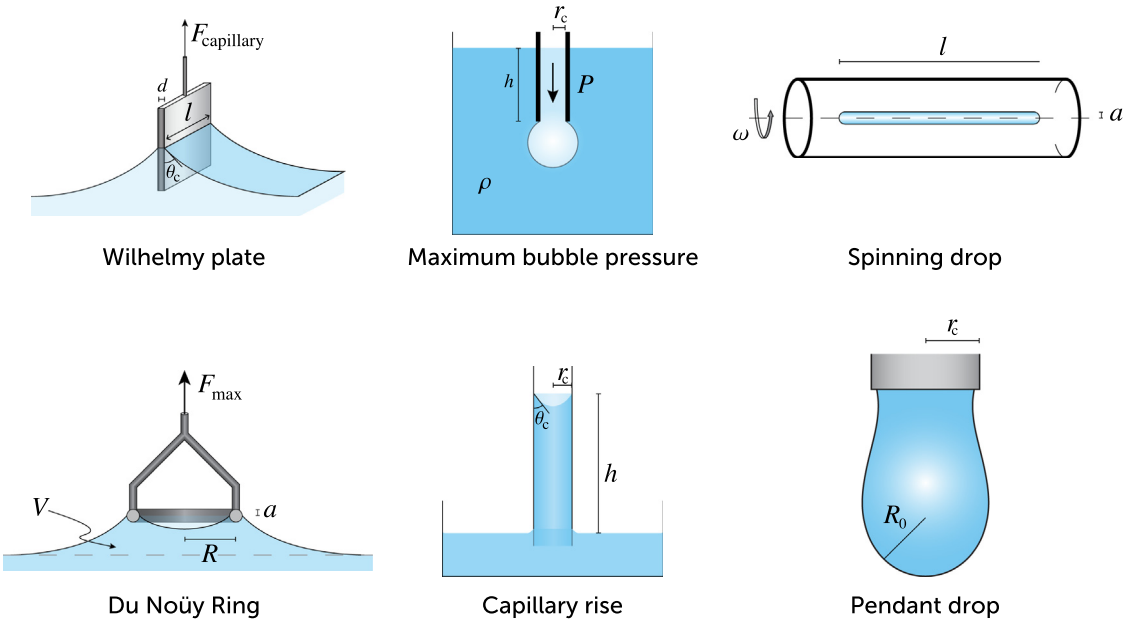


**Fig. 1.** Schematics of various experimental techniques used to determine interfacial tension.

Rotenberg et al. [14]. The method proposed by Rotenberg et al. [14] regards the position of the apex as an unknown quantity that is determined simultaneously with the apex radius and 'shape parameter' (Bond number), in turn increasing the precision. The advances in computational methods of the ADSA (axisymmetric drop shape analysis) algorithms developed by Neumann and co-workers are detailed by Hoorfar and Neumann [16].

Jennings and Pallas [17] improved upon the method of Rotenberg et al. [14] by implementing 'rotational discrimination', which may be regarded as a modified Gauss–Newton method, to perform the optimisation routine, drastically reducing the computational time requirement. In addition, this work provided a detailed error analysis that gives accurate, conservative intervals associated with the experimental uncertainty.

Although Gauss–Newton optimisation is widely used and can offer extremely fast convergence between the experimental and fitted droplet profile, it can fail to converge if an insufficiently accurate initial guess for the theoretical profile is provided. An alternative optimisation routine is the Levenberg–Marquardt algorithm [18,19], which essentially interpolates between Gauss–Newton and steepest descent. This routine is commonly used in pendant drop routines as it combines the speed of Gauss–Newton with the robust convergence of steepest descent [20].

Hoorfar and Neumann [16] also provided a useful critical scrutiny of the technique in terms of both experimental setup and fitting software, including important discussions of potential sources of error and dynamic effects. The issue of reduced fidelity at low Bond number is noted here, along with issues of optical aberration introduced by the experimental components. Alvarez et al. [21] showed that alternative computational algorithms for fitting the theoretical drop profile to the experimental image may improve matters somewhat at low Bond numbers, although this does not overcome the fundamental physical limitation itself, that the error grows without bound as the Bond number approaches zero. The physical reason for this is simply that the drop is barely deformed away from a sphere, and this deformation is therefore too small to accurately quantify. An alternative approach to obtaining surface tension from droplet profiles using the Galerkin finite element method was proposed by Dingle et al. [22], demonstrating comparable precision, although this method may be more computationally demanding.

More recently, the pendant drop method has been further developed to include a wider variety of drop configurations, from capillary bridges between two parallel plates [23–25] to compound pendant drops [26] formed when a spherical particle is attached to a pendant drop. These configurations have provided a significant extension to pendant drop tensiometry as they enable the method to accurately measure interfacial tensions for Bond numbers as low as zero [26].

This article provides a technical review of the processes involved in the fitting of experimental images to obtain interfacial tension using pendant drop tensiometry, covering theoretical requirements along with experimental details, a thorough investigation of errors and limitations, and the introduction of a new dimensionless parameter that accurately characterises measurement precision. A detailed derivation of the associated theory is included in the Appendices.

The closed-source and commercial nature of most pendant drop tensiometry fitting routines has perhaps stifled development of the technique by the broader colloid science community, and so in addition, we provide a fully featured, free and open-source pendant drop tensiometry software written in the Python language, with the intention that this will facilitate renewed research and development of the technique itself.

## 2. Experiment

The experimental apparatus required for pendant drop tensiometry is almost trivial in its simplicity: all that is required is a needle, a camera, and a light source. A basic experimental setup is shown in Fig. 2a.

Though the experimental setup is relatively simple, a number of factors must be considered to ensure that the image is of sufficient quality for precise determination of interfacial tension. Crucially, the light source must be diffused to ensure that no optical aberrations occur at the drop periphery, and spurious reflections from the drop interface arising from other sources (*e.g.* overhead lighting) must be avoided. Similarly, the drop image as acquired at the digital camera sensor must be undistorted by lensing effects, and analysis is greatly simplified by a homogeneous image background. A typical image that is well suited to fitting is shown in Fig. 2b.

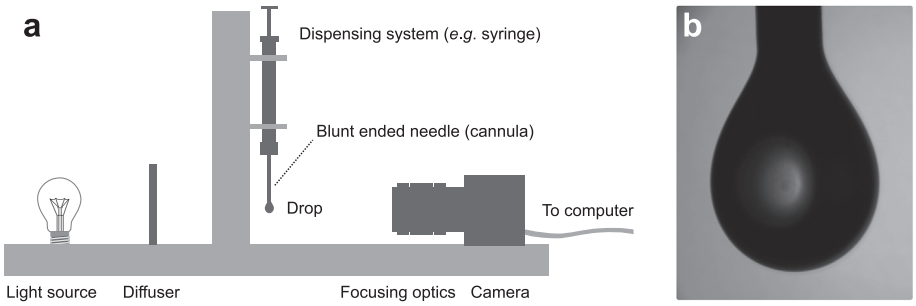


**Fig. 2.** (a) A basic experimental setup for pendant drop tensiometry; (b) a typical drop image as acquired by a digital CMOS camera.

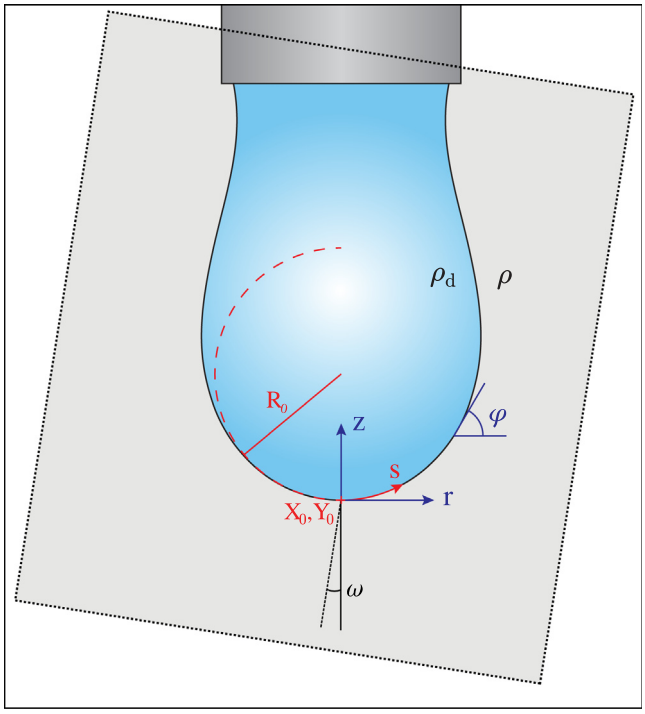


**Fig. 3.** A schematic of a pendant drop below a needle. The shaded region represents the image area captured by the camera, which is not necessarily aligned perfectly with the drop. The annotations show the associated variables used in the computational routine to determine the Bond number, and thus the interfacial tension.

Finally, the requirement of droplet axisymmetry is central to obtaining precise measurements of interfacial tension, and thus the needle must be absolutely vertical (*i.e.* parallel to gravity).

In particular, the drop size needs to be of adequate size to ensure that gravitational effects are non-negligible. If the gravitational effects are too small, then the Bond number is close to zero, leading to problems associated with the fitting algorithm (a detailed discussion of this can be found in Section 5.3). The Bond number scales as $\mathrm{Bo} \sim R_0^2$, hence larger drops will give a larger Bond number (assuming that the density difference is non-negligible), resulting in less chance of fitting problems.

An additional concern is the problem of droplet oscillation induced by both vibrations that originate externally to the experimental apparatus, and also air currents. The deleterious effects of the former can be minimised with an anti-vibration table, whereas the latter are readily avoided by performing the measurement in a sealed cuvette. The inertial damping effect of a liquid continuous phase is such that vibrations are significantly less problematic when measuring interfacial tensions for liquid–liquid systems.

## 3. Theory

A pendant drop at equilibrium obeys the Young–Laplace equation, which relates the Laplace pressure across an interface with the curvature of the interface and the interfacial tension $\gamma$:

$$\gamma\left(\frac{1}{R_1}+\frac{1}{R_2}\right) = \Delta P \equiv \Delta P_0 - \Delta\rho g z \tag{1}$$

where $R_1$ and $R_2$ are the principal radii of curvature; $\Delta P \equiv P_{\mathrm{in}} - P_{\mathrm{out}}$ is the Laplace pressure across the interface; $\Delta\rho = \rho_d - \rho$ is the density difference (see Fig. 3); and $\rho_d$ and $\rho$ are the drop phase density and continuous phase density respectively. This can be written in terms of a reference pressure $\Delta P_0$ at $z = 0$ and a hydrostatic pressure $\Delta\rho g z$. By taking advantage of axisymmetry, Eq. (1) can be expressed in terms of the cylindrical coordinates $r$ and $z$, together with the tangent angle $\varphi$, as shown in Fig. 3. Thus, the Young–Laplace equation can be obtained as a coupled set of dimensionless differential equations in terms of the arc length $s$ measured from the drop apex,

$$\frac{\mathrm{d}\varphi}{\mathrm{d}\bar{s}} = 2 - \mathrm{Bo}\,\bar{z} - \frac{\sin\varphi}{\bar{r}} \tag{2a}$$

$$\frac{\mathrm{d}\bar{r}}{\mathrm{d}\bar{s}} = \cos\varphi \tag{2b}$$

$$\frac{\mathrm{d}\bar{z}}{\mathrm{d}\bar{s}} = \sin\varphi \tag{2c}$$

where the bar indicates dimensionless quantities scaled by $R_0$, the radius of curvature at the drop apex. All variables are defined in Fig. 3. It should be noted that the Young–Laplace equation can only be solved analytically for the trivial case where the droplet profile is a sphere, and this solution is inconsequential for pendant drop tensiometry as it corresponds to $\gamma \to \infty$. In other cases, the equations must be numerically solved. In Eq. (2), Bo denotes the Bond number, defined by

$$\mathrm{Bo} \equiv \frac{\Delta\rho g R_0^2}{\gamma}. \tag{3}$$

The associated boundary conditions are

$$\bar{r} = 0, \quad \bar{z} = 0, \quad \varphi = 0 \quad \text{at} \quad \bar{s} = 0. \tag{4}$$

The shape of the pendant drop is therefore dependent on a single dimensionless quantity, the Bond number, Bo. If the Bond number associated with a pendant drop can be determined together with the drop radius $R_0$ at the apex, the interfacial tension $\gamma$ is then readily obtained from Eq. (3). This is the theoretical essence of the pendant drop technique.

The fitted Young–Laplace solution can also be used to give additional data, such as drop volume $V_{\mathrm{d}}$ and drop surface area $A_{\mathrm{d}}$, which are defined as

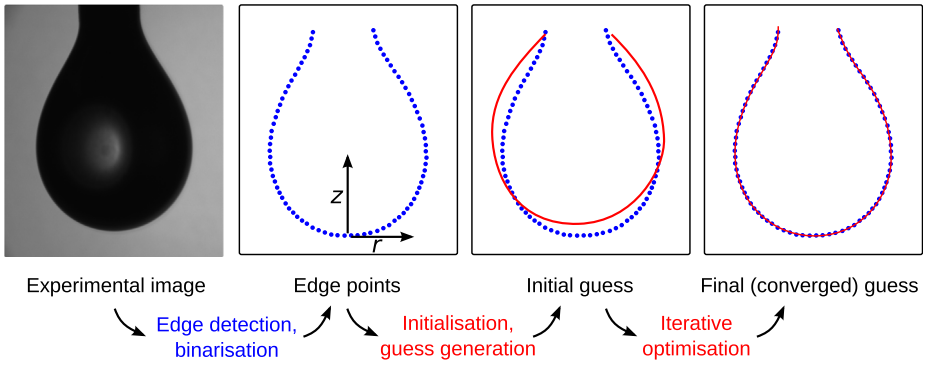


**Fig. 4.** Schematic of the pendant drop tensiometry process, going from a raw experimental image to a fitted solution from which $\gamma$ can be obtained.

$$V_d = \pi \int \bar{r}^2 \sin\varphi \, d\bar{s}, \quad A_d = 2\pi \int \bar{r} \, d\bar{s}. \tag{5}$$

This allows further interfacial data to be extracted. For example, tracking the drop volume over time allows quantification of the drop evaporation rate.

## 4. Method overview

Although the pendant drop method is conceptually straightforward, fitting the Young–Laplace equation to an experimental image requires a complex computational routine. This procedure can be divided into two subroutines: firstly, the drop profile is extracted from an experimental image, and secondly, the Young–Laplace equation is iteratively solved to find the physical parameters that most precisely describe the extracted drop profile using optimisation techniques. The process is shown schematically in Fig. 4. Determining the drop profile from an experimental image is a standard problem in edge detection, and various methods have been reviewed and discussed previously [16]. The Canny edge detector [27], wherein image intensity gradients are analysed using a multi-pass approach, is widely used due to its robust nature over a range of contrast conditions.

Once a suitably precise experimental droplet profile has been obtained as $r,z$ coordinates, the theoretical pendant drop profile is fitted to the extracted experimental data by minimising the sum of squared residuals

$$S = \sum_{i=1}^{n} e_i^2 = \sum_{i=1}^{n} \min_{\bar{s}} \left\{ e_i^r(\bar{s})^2 + e_i^z(\bar{s})^2 \right\}, \tag{6}$$

where the $i$th residual, $e_i$, is defined as the minimum Euclidean distance between the data point $(r_i, z_i)$ and any point on the theoretical drop profile $(r(s), z(s))$. The squared residual can be expressed in terms of a horizontal $e_i^r$ and a vertical $e_i^z$ component, which are defined in Eqs. (B.2a) & (B.2b).

The required fitting routine can be recast as a minimisation of the non-linear function $S(\boldsymbol{\beta})$, where $\boldsymbol{\beta} = \{X_0, Y_0, \omega, R_0, \mathrm{Bo}\}$ are the parameters that determine the theoretical drop profile (Fig. 3). Here $X_0$ and $Y_0$ are the coordinates of the droplet apex, and $\omega$ is the rotational angle of the experimental image relative to gravity. The Levenberg–Marquardt–Fletcher automated optimisation (LMF–AO) algorithm [18,19,28] is particularly well suited to this fitting routine as it combines the speed of Gauss–Newton with the stability of steepest descent. LMF–AO updates the parameter set $\boldsymbol{\beta}$ according to

$$\boldsymbol{\beta}^{(k+1)} = \boldsymbol{\beta}^{(k)} + \boldsymbol{\delta} \tag{7}$$

where $\boldsymbol{\delta}$ is determined by solving

$$\left(\mathbf{J}^{\mathrm{T}}\mathbf{J} + \lambda \, \mathrm{diag}(\mathbf{J}^{\mathrm{T}}\mathbf{J})\right)\boldsymbol{\delta} = -\mathbf{J}^{\mathrm{T}}\boldsymbol{e} \tag{8}$$

where $\boldsymbol{e}$ is the vector of residuals and $\mathbf{J}$ is the Jacobian matrix. Details of how the Jacobian matrix is calculated is found in Appendix B, and details of the optimisation routine for determining the arc-length at which the associated Euclidean distance is minimised at each point is given in Appendix C.

In Eq. (8), the value of $\lambda$ is chosen at each step to ensure convergence. In this work the value of $\lambda$ is set according to Fletcher's criteria [28], see Appendix A for details.

The parameters $\boldsymbol{\beta}^{(k)}$ can be updated according to Eqs. (7) and (8) until one of the following convergence criteria are met:

i. convergence in the objective function, $S/(n-m+1) < \mathrm{tol}_1$, or
ii. convergence in the parameters, $\max_j \mid \beta_j^{(k+1)} - \beta_j^{(k)} \mid < \mathrm{tol}_2$, or
iii. convergence in the gradient, $\max_j \mid \mathbf{J}_{ij}^{\mathrm{T}} e_i \mid < \mathrm{tol}_3$,

with the addition of a maximum number of allowed iterations. Here $n$ and $m = 5$ are the number of data points and the number of fitted variables respectively, and $\mathrm{tol}_{1,2,3}$ are tolerances typically of order $10^{-4} - 10^{-7}$.

In summary, the optimisation routine proceeds as follows:

0. The parameters are initialised by fitting a circle to experimental data points that define the bottom 10% of the drop, giving initial guesses for both the centre $(X_0, Z_0)$ and radius $R_0$. The rotation $\omega$ is initially set to zero. The Bond number is initialised from an expression based on the work of Andreas et al. [11].[4] Further, the parameter $\lambda$ is initialised as 0.
1. The solution to the Young–Laplace equation is generated based on the current values of $\boldsymbol{\beta}^{(k)} = \{X_0^{(k)}, Y_0^{(k)}, \omega^{(k)}, R_0^{(k)}, \mathrm{Bo}^{(k)}\}$.
2. For each experimental data point $i$, the arc-length $\bar{s}_i$ that minimises the Euclidean distance $e_i$ is calculated (Appendix C).
3. The Jacobian matrix entry $J_{ij}$ is calculated for each experimental data point $i$ and parameter $j$ (Appendix B).
4. Eq. (8) is solved to find $\boldsymbol{\delta}$.
5. Eq. (7) is solved to find the updated parameter set $\boldsymbol{\beta}^{(k+1)} = \{X_0^{(k+1)}, Y_0^{(k+1)}, \omega^{(k+1)}, R_0^{(k+1)}, \mathrm{Bo}^{(k+1)}\}$, and a new estimate for $\lambda$ is generated (Appendix A).
6. Steps 1 – 5 are repeated until convergence is reached.

[4] This initial guess exists only if the drop height is greater than $2R_0$. If this condition is not met, we have found that a naive guess for the Bond number ($\mathrm{Bo} = 0.15$, say) is generally sufficient for quick and accurate measurements.

**Table 1**
Comparison of a range of systems measured using the current implementation of pendant drop fitting routines with accepted literature values. Measurements were made at ambient laboratory temperature which was thermostatically controlled to 22 °C. The errors in experimental values represent the standard deviation in 20 independent measurements.

| Droplet phase | Continuous phase | Experimental IFT mN m$^{-1}$ | Literature IFT mN m$^{-1}$ | Refs. |
|---|---|---|---|---|
| Water | Air | 72.68 ± 0.18 | 72.75 ± 0.36[a] | [29] |
| Glycerol | Air | 64.39 ± 0.38 | 63[b] | [30] |
| Perfluorohexane | Water | 54.80 ± 0.28 | 55 ± 1.1[b] | [31] |
| CTAB[c] (10 mM) | Air | 34.82 ± 0.23 | 37[b,d] | [32] |
| Toluene | Air | 28.20 ± 0.36 | 28.52[a] | [33] |
| *n*-Tetradecane | Air | 25.86 ± 0.34 | 26.56[a] | [33] |
| Water | Ethyl acetate | 6.63 ± 0.02 | 6.8[b] | [34] |

[a] At 20 °C.
[b] At 25 °C.
[c] Cetyltrimethylammonium bromide.
[d] At the CMC, 0.84 mM.

## 5. Results and limitations

### 5.1. Equilibrium and dynamic interfacial tension

One of the most appealing features of pendant drop tensiometry is that unlike the majority of other tensiometry methods, there is no mechanical or electronic transducer or force sensor that must be calibrated. Gravity is responsible for the deformation used to quantify interfacial tension, and gravitational acceleration is broadly constant (with minor and easily quantified variations due to location). To demonstrate the capabilities of the current implementation of pendant drop fitting routines, a number of exemplar model systems are used that cover a range of Bond numbers and interfacial tensions. A summary of these results is provided in Table 1.

It is seen that the current implementation offers both high accuracy when compared to literature values using a range of techniques and different systems. The result for CTAB at 10 mM is significantly lower than the literature value at the critical micelle concentration (0.84 mM), however continued decrease in surface tension after the CMC is well known [35], possibly due to residual impurities such as alcohol remaining from the surfactant synthesis, or non-Gibbs effects resulting from incomplete dissociation of the surfactant and counterion. We chose this system to exemplify a typical challenging surfactant system where the drop is difficult to sustain on the needle.

### 5.2. Dynamic effects

Adsorption kinetics and dynamic surface tension, particularly of low molecular weight surfactants, have been a topic of active research for many decades, with relevance to a vast number of processes from emulsification to printing, coating and mineral flotation [36]. Pendant drop tensiometry is not conventionally ideal for measurement of fast dynamic interfacial processes (*i.e.* time-steps of less than ≈1 s), as it relies upon an equilibrium condition under which the Young–Laplace equation is valid. At faster droplet creation rates, fluid flow and inertial effects invalidate this assumption. Maximum bubble pressure is preferred for measurement times down to ≈10 ms [37], and below this, more demanding measurements such as the oscillating jet method must be used [38]. Pendant drop tensiometry however is adept at measuring interfacial tensions over long periods of hundreds or even thousands of seconds. However, caution must be taken to avoid significant changes in parameters over time.

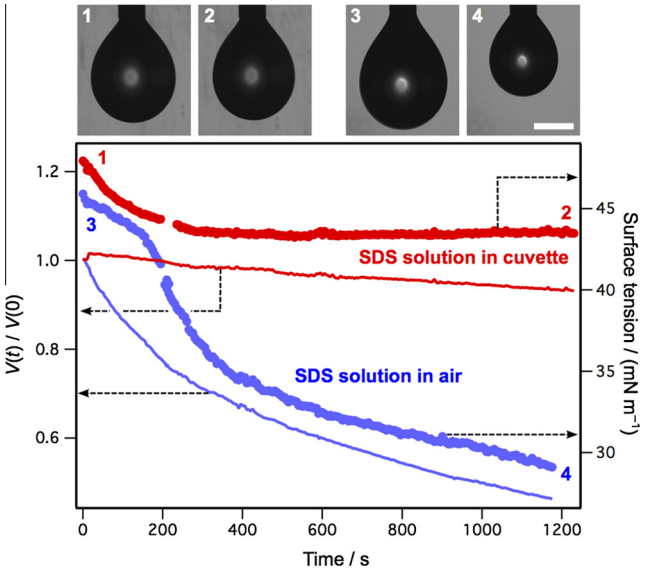


**Fig. 5.** The apparent surface tension and measured droplet volume as a function of time for a 4 mM solution of sodium dodecylsulfate (SDS), measured as a 'naked' drop in air, or enclosed in a gas-tight cuvette with a droplet of solution at the bottom. The images at the top show the drops at the start and end of each measurement; the white scale bar applies to all images and represents 1 mm.

It is an unavoidable feature of pendant drop tensiometry that the droplet will always be thermodynamically driven to evaporate (or dissolve) at a rate controlled by surface area, diffusivity and humidity, as its curved interface increases the chemical potential of its contents [39,40]. For liquid–liquid interfacial tensions where liquid pairs of low mutual solubility are dealt with, this problem is minimal and can be neglected. However, for droplets of comparatively volatile solvent in air (including water drops), evaporation is a significant problem that must be addressed or accounted for [39]. Thus, measurement of droplet volume concomitantly with interfacial tension is valuable and necessary.

The pitfalls associated with long measurement times and waiting for equilibrium to be attained are shown in Fig. 5. In this experiment, the surface tension of a droplet of sodium dodecylsulfate (SDS) solution at a concentration of 4 mM is measured over time. In one set of measurements, the drop is freely exposed to the surrounding atmosphere; in the other, the needle and drop is sealed in a gas-tight cuvette containing a sessile drop of the experimental solution at the bottom. The purpose of this latter setup is to create an equilibrium humid atmosphere around the drop to slow its evaporation. From Henry's law we assume that a pendant drop is always in equilibrium with an adjacent layer of saturated vapour, and thus using a sealed atmosphere to maintain this significantly inhibits further evaporation [39].

From Fig. 5, the difference between the free and sealed environments is clear. In the sealed case, an equilibrium surface tension is rapidly attained, and over the course of 1200 s, the droplet volume only decreases by 3%. For the free drop exposed to the laboratory atmosphere (relative humidity measured at 36%), the surface tension continually decreases, and over the same time period, the droplet volume decreases by $>$ 50%. This example is particularly stark as the surfactant concentration was chosen to be below, but close to the CMC. It is likely that evaporation from the drop in the unsealed case causes a local increase in concentration within the drop, driving more surfactant to the interface and lowering the surface tension.

As an interesting aside, when the concentration of SDS within the droplet increases, a concentration gradient is set up with the remaining SDS solution 'reservoir' in the needle and syringe above.

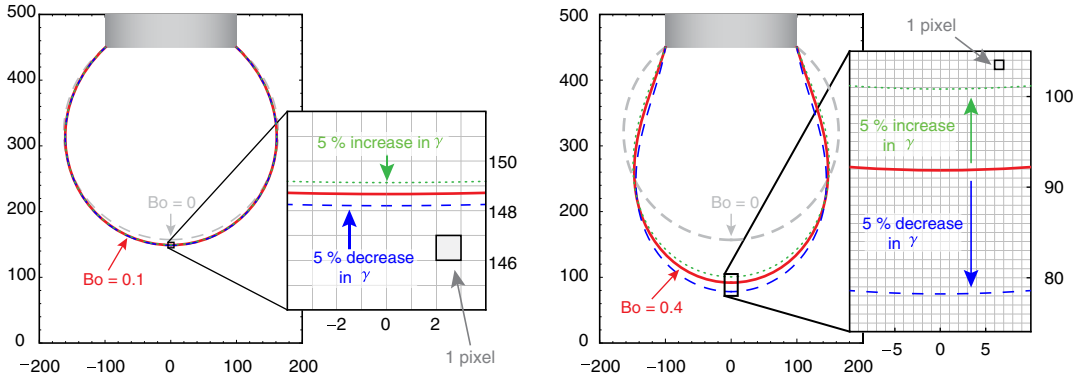


**Fig. 6.** A schematic of two drops of the same drop volume, but different Bond numbers. The drop on the left has a Bond number of 0.1, while the drop on the right has a Bond number of 0.4, these interfaces are shown in solid red. In each case the interfacial tension is perturbed by 5%, with a 5% increase in $\gamma$ shown in dashed blue and a decrease in dotted green. The inset in both images is a zoomed in region near the drop apex, with the grid line spacing equal to the pixel density of the Sony IMX035 CMOS image sensor used in these experiments. When the Bond number is small, the interfaces are only slightly perturbed, demonstrating the reduced sensitivity in this regime.

This will eventually tend to equilibrate at a diffusion controlled rate; this complex coupled problem has not yet been explored to the authors' knowledge.

### 5.3. Physical limitations

#### 5.3.1. Low Bond number systems

Although pendant drop tensiometry provides a simple and elegant method for determining interfacial tension, the accuracy of the approach is dependent upon a number of factors, including image quality and drop shape. It is well known that the method is inaccurate when the Bond number is small [16], however this is not a very useful guide because the Bond number of any particular experimental configuration is not known *a priori*. The fidelity with which interfacial tension can be obtained depends on how accurately the Bond number can be determined from experimental data. A small Bond number implies that the interfacial forces dominate the gravitational forces, with the resulting drop profile only slightly deformed away from sphericity, as illustrated in Fig. 6. In this regime, the sensitivity of the method is inherently low, since a small change in the drop profile results in a large change in the apparent interfacial tension. Sometimes this limitation may be circumvented by making a larger drop, although if the droplet and continuous phases have similar densities, this may not be possible. In the latter case, modifications need to be made to the experimental setup to accurately access the interfacial tension when the associated Bond number is very small [26].

#### 5.3.2. Drop volume effects

In order to determine the effects of droplet volume on measurement sensitivity, a series of synthetic drops were formed for a range of needle widths and Bond numbers. The system considered is a water drop of density $\rho = 10^3$ kg/m$^3$ suspended in air (with negligible density), and a surface tension of $\gamma = 72.6$ mN/m. For each needle width considered, a number of theoretical drops were generated from the solution of the coupled differential equations defined in Eq. (2) with associated boundary conditions (Eq. (4)). The Bond numbers were chosen to span the physically realisable range for each needle width. Once a theoretical drop was generated, 100 randomised data sets of the drop profile were created by rotating the drop profile by a random angle in the range $-5^\circ \leqslant \omega \leqslant 5^\circ$ , and displacing it by a random offset amount in the range $-0.1R_0 \leqslant X_0, Y_0 \leqslant 0.1R_0$. Each randomised droplet data set was then binarised by rounding each edge coordinate value to an integer, such that each pixel represents 8.26 μm. The resulting pixels form the drop profile that correspond to discrete edge detection with no error. The resolution has been deliberately chosen to be coarser than typical cameras used for pendant drop tensiometry, in order to rigourously test the computational routine. Further, the angle range chosen to randomise the drop profiles is well above that expected for a typical experimental apparatus.

Once the 100 randomised synthetic drop profiles were formed, the routine outlined in this paper was used to fit the Young–Laplace equation to each drop, with the interfacial tension calculated from the fitted parameters. The results of the calculations are shown in Fig. 7a), for each of the randomised profiles generated. Also depicted are some sample images of the theoretical drop profiles, and the corresponding 'true' values of Bond number and surface tension. For each needle width considered, the fitting accuracy increases as the true Bond number becomes larger, and the spread of measured, 'apparent' values of Bond number and surface tension become negligible for each theoretical drop considered. Conversely, at low true Bond number, the variability of the apparent Bond number and apparent surface tension becomes extremely large. For the lowest true Bond number considered for the needle diameter of 1.65 mm, Bo = 0.09, the fitted Bond number varies from 0.06 to 0.11, highlighting the futility of using the Bond number as the sole measure of the accuracy of any particular measurement.

Intriguingly, as the needle width decreases, the minimum true Bond number required for accurate calculation also decreases, despite the magnification remaining constant. For example, drop profiles *i* (0.72 mm needle diameter) and *ii* (0.51 mm needle diameter) are of similar true Bond number (0.04 and 0.048 respectively); however the variability in the fitted parameters is much less for the drop formed using the smaller needle. The variation of accuracy with needle width suggests that an appropriate choice of non-dimensional number will result in collapse of the data presented in Fig. 7a) to a universal solution independent of needle diameter. To this end, we introduce a non-dimensional number that scales the drop volume $V_d$ (which can be calculated with Eq. (5)) by the theoretical maximum drop volume $V_{max.}$ that can be sustained for the system. We term this parameter the Worthington number,[5] Wo, written as

$$\mathrm{Wo} = \frac{V_d}{V_{max.}}. \tag{9}$$

One appropriate choice of $V_{max.}$ could be the weight of a drop that detaches from the needle for a given interfacial tension. This is

[5] In honour of Arthur Mason Worthington FRS (1852–1916), who originally proposed that the shape of pendant liquid drops could be used to obtain their surface tension [4].

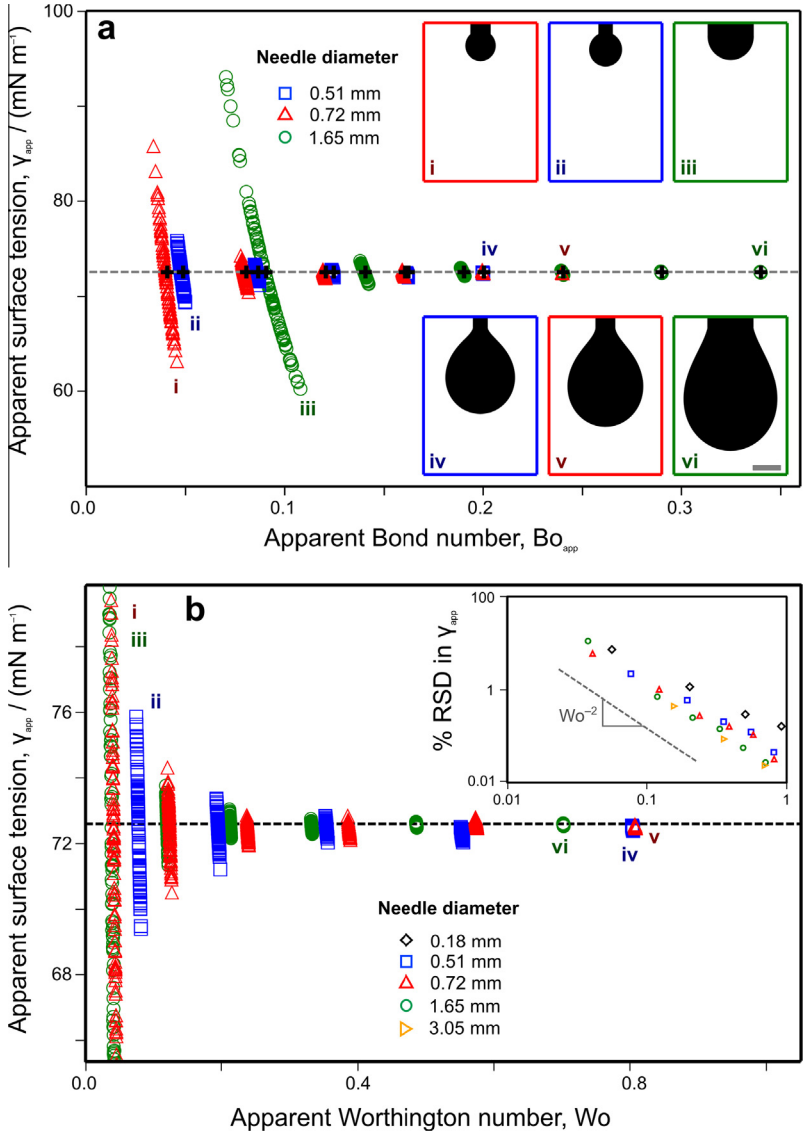


**Fig. 7.** (a) Apparent surface tension and Bond number data obtained from fitting synthetically generated and randomised droplet profiles with different initial volumes and needle widths. Each cluster of points represents 100 independent measurements of drops obtained by randomising the same theoretical drop profile. The dashed line and the black symbols (+) indicate the 'true' surface tension and 'true' Bond numbers respectively of each theoretical drop profile. The inset droplet profile images correspond to the labelled data sets; the inset scale bar corresponds to all images and represents 1 mm. (b) The same data as shown in a), but now surface tension is represented as a function of the Worthington number, Wo that accounts for the ratio of droplet volume to the critical droplet volume for each needle width. The inset shows the % relative standard deviation (%RSD) for each measurement set as a function of Wo. Note that on the log axes, the precision scales with $Wo^{-2}$. The black diamonds represent data sets for a needle width of 0.18 mm, demonstrating that for sufficiently small drops, low Bond number does increase error somewhat due to the minimal deformation that the drops experience.

the basis for drop-weight tensiometry, first demonstrated in 1864 by Tate [41]. However, the actual detachment volume depends on the precise shape of the needle tip and its surface chemistry, and is non-trivial to calculate, requiring correction factors that account for the fact that some of the drop is left behind at the needle during the detachment process [42,43]. Another appropriate choice is the maximum droplet volume that can be theoretically sustained by the needle, defined by Harkins and Brown as the 'ideal drop' from Tate's original treatise[6] [41–43]:

$$V_{\max.} = \frac{\pi D_n \gamma}{\Delta\rho g}, \tag{10}$$

where $D_n$ is the needle diameter. The advantage of expressing the maximum drop volume in the form of Eq. (10) lies in its trivial calculation. Thus, the Worthington number can be written

$$\mathrm{Wo} = \frac{\Delta\rho g V_d}{\pi\gamma D_n}. \tag{11}$$

The Worthington number in this form can also be considered as a Bond number with length scale $\sqrt{V_d/\pi D_n}$.

In Fig. 7b, we replot the apparent surface tension for all synthetic drop profiles considered as a function of the apparent Worthington number. This makes it clear that scaling these data by critical drop volume gives a much more accurate indication of measurement precision. The inset to Fig. 7b shows the % relative

[6] Tate's 'ideal drop' definition is a somewhat naive approximation of the maximum drop size sustainable for any particular needle width and interfacial tension, however it is a simple approximation that gives a reasonable estimate of the actual theoretical maximum drop size as calculated from the Young–Laplace equation (which requires a complex iterative computational routine).

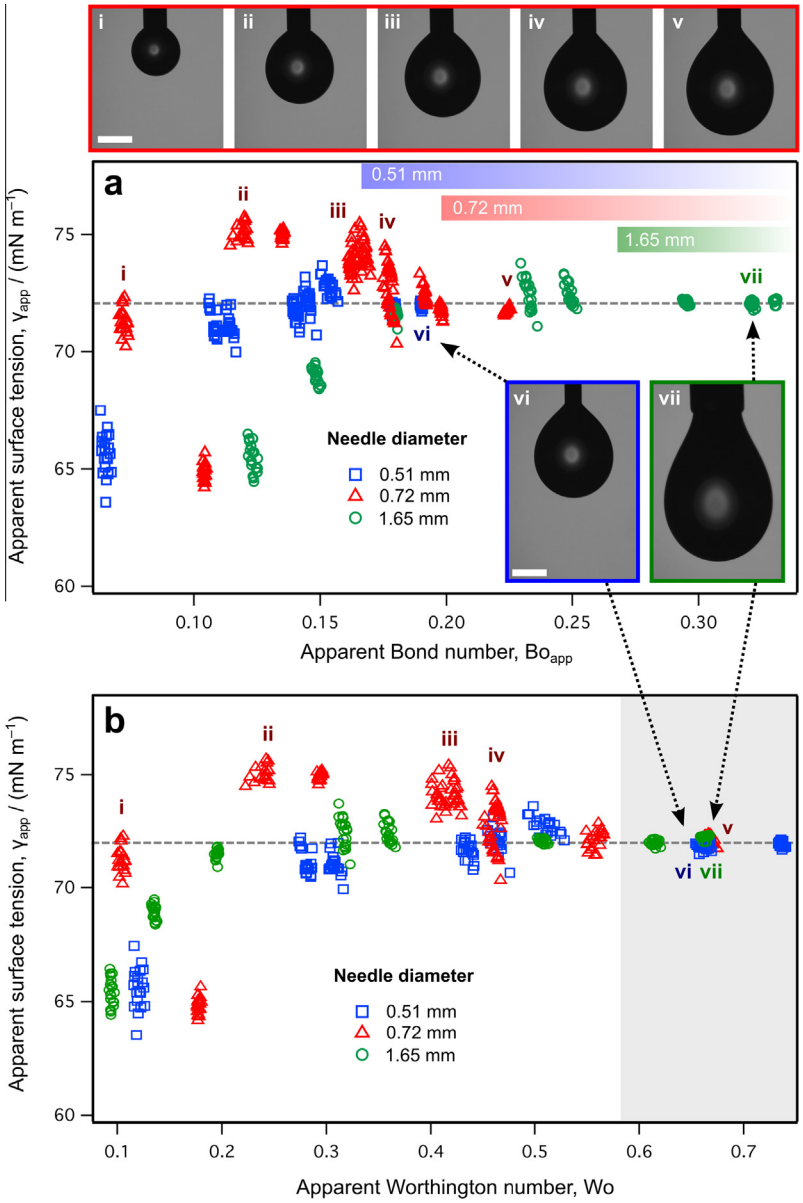


**Fig. 8.** (a) The apparent surface tension and Bond number obtained from fitting experimental water drops of different volumes generated at needles of different widths. Each cluster of points represents 20 sequential measurements of the same droplet over time. The inset images show droplet shapes from selected data sets as labelled, where the scale bar applies to all images and represents 1 mm. The dashed horizontal line represents the literature value for the surface tension of water at 22 °C, and the coloured bars at the top of the panel show the approximate regions in which the different needles can be used to obtain data with high precision (as characterised by a mean surface tension <0.2 mN/m from the accepted value and a standard error across the data set of <1%). (b) The same apparent surface tension data as shown in panel a), but now represented as a function of the Worthington number, Wo. The grey shaded region represents data that have a mean <0.2 mN/m from the accepted surface tension value and a standard error across the data set of <1%.

standard deviation (%RSD) in surface tension as a function of Worthington number, demonstrating a characteristic relationship whereby %RSD $\propto$ Wo$^{-2}$. This relationship should be useful for estimating characteristic errors in fitted parameters for a given optical setup, with only two or three points required to 'calibrate' the %RSD.

The data points represented by black diamonds in the inset represent drops generated from a very small needle (0.18 mm), indicating that in extreme circumstances, low Bond number – *i.e.* insufficient deformation – does increase the error in fitted parameters. However, for the majority of data presented here for typical needle sizes used in experiments, the Worthington number is a much more meaningful measure of the characteristic precision.

We explore the issue of fitting accuracy as a function of drop size and Bond number experimentally in Fig. 8. As observed in the theoretical data shown in Fig. 7, the measurement precision is a strong function of droplet volume, with Bond number representing a secondary correction. This contradicts previous studies that do not account explicitly for droplet volume, considering Bond number alone to be the primary factor in determining measurement precision for a given system [16,21]. These effects are particularly evident when the data are scaled by the Worthington number, Wo (Fig. 8b) and the data sets showing effective precision (as evidenced by the spread of fitted surface tension values) collapse to the same functional form. Of particular note are the two drops labelled *vi* and *vii*, which show almost identical measurement precision across their data sets but have Bond numbers that differ by almost a factor of two. This clearly indicates the importance of relative droplet volume and needle diameter in measurement precision for pendant drop tensiometry.

These observations demonstrate that the Worthington number can effectively be used as a post-measurement 'sanity check' to give an important indication of the likely measurement precision. Although it is possible to use known or assumed values to perform an *a priori* assessment of the best experimental parameters, we envisage that it will be more useful as an *a posteriori* benchmark of measurement quality. However, if a reasonable guess of interfacial tension can be made, calculation of Wo may provide a useful method for assessing the most appropriate needle size for an experiment. Across the Bond number range typically dealt with in pendant drop tensiometry, Bond number alone is a poor indicator of precision, and should be replaced by Wo. Clearly at very low Bond numbers ($Bo < 0.1$) the physical limitation of poorly-deformed drops still applies, although this can be overcome by introducing additional interfacial deformation [26].

## 6. Current research and future directions

Pendant drop tensiometry remains an active area of research, with recent significant extensions to the technique and systems to which it can be applied. The concept of measuring contact angle and interfacial tension simultaneously is appealing for many applications, particularly where fluids are being selected for (micro) fluidic handling applications. Recent work has extended the pendant drop technique to enable measurement of contact angle, by the introduction of a secondary solid surface in the form of a flat substrate [23–25] or particle [26]. In certain circumstances, this has the added benefit of applying a secondary force that allows measurement of interfacial tension at low or even zero Bond numbers [26]. This allows measurement not only in density matched systems for emulsion studies, but also at much smaller fluid volumes, which is of particular interest when biological samples are handled that may be particularly scarce or valuable.

Another recent development in the field is the use of pendant drop tensiometry to study dilational rheology (specifically the dilational stress modulus) of adsorbed layers at droplet interfaces [44]. By applying a small volume oscillation to the droplet, information on the elasticity and response of the surface layer can be obtained [45,46,44], building from earlier work where the droplet volume was changed incrementally [47]. This has significant potential in the study of polymers, proteins and other biomolecules at interfaces, although care must be taken to properly account for the effects of fluid flow and interfacial shear in such experiments [48,49]. By monitoring a shrinking drop with an adsorbed insoluble monolayer at the interface, surface pressure isotherms akin to those from Langmuir trough experiments can be obtained [50].

With high-frame rate cameras becoming significantly more affordable in recent years, it is likely that dynamic systems become accessible using pendant drop techniques. However, the added complication is that dynamic changes in fluid volume are accompanied by complex inertial flow fields that may inhibit analysis using the equilibrium Young–Laplace equation. Holistic models that account for interfacial deformation, fluid flow and interfacial tension must therefore be developed to access shorter time-scale information. Such modelling is now commonplace in understanding flows in microfluidics [51], colloidal atomic force microscopy [52] and film interferometry experiments [53], and as such could potentially be extended to dynamic pendant drop studies.

## 7. Conclusion

The pendant drop method is a powerful technique that can be used to accurately determine the interfacial tension. While the modern pendant drop computational routine was developed over three decades ago, [14] research into the methodology has been slow, possibly due to commercial interests and a lack of availability of the computational resources.

In this work we have provided a comprehensive discussion of the theoretical background to the technique, highlighting also its limitations. The issue of reduced accuracy at low Bond numbers is a fundamental physical limitation [16], although it can be overcome using modifications to the technique where an extra interface is included in the form of a solid surface or particle [23–26]. However, we find that in counterpoint to literature reports [16,21], this is not the primary source of error in most practical pendant drop experiments. In fact, the drop volume is an overriding criterion in determining measurement precision, with droplets closest to the critical detachment volume offering the most accurate and precise measurements. We introduce a new non-dimensional quantity, the Worthington number, Wo that scales from 0 to 1, to account for this volume effect, where large values of Wo indicate the greatest precision. This can be used as a post-measurement check to ensure that data obtained are reasonable and likely to be sufficiently accurate.

In addition, we have developed an open-source Python program that facilitates accurate acquisition of surface and interfacial tension data, and further provides opportunities to develop and expand upon the technique itself. We intend that this will stimulate further research interest in pendant drop tensiometry as well as providing a valuable tool for surface and colloid scientists.

## 8. Experimental

Solvents were purchased from Sigma or Chem Supply (Australia) Ltd, all 99% purity or greater, and were further purified by distillation and/or column chromatography over magnesium silicate before use. Sodium dodecylsulfate (SDS) and cetyltrimethylammonium bromide (hexadecyltrimethylammonium bromide, CTAB) where obtained from Chem Supply (Australia) Ltd (99% purity) and used as received. Needles used were regular medical blunt-tipped cannulae (Monoject) in gauges 16, 18, 22 and 25, with nominal outer diameters of 1.650, 1.270, 0.718 and 0.514 mm respectively. Their widths were measured independently using a micrometer and the precise value used in calculations. Syringes used were standard Luer-lock gas-tight glass syringes from Hamilton Corporation. The cameras used in the experiments shown here were both Flea3 CMOS imaging cameras from Point Grey (Richmond, BC, Canada), equipped with either a Sony IMX035 CMOS, 1/3'' sensor or On Semi VITA1300 CMOS, 1/2'' sensor. The lens used was a C-mount CCTV lens, $F = 1.4$, utilising a macro tube to provide the necessary zoom level. Backlighting was from a white LED (CREE C503C-WAS) diffused with a ground-glass disc. The optical setup was tested extensively for image aberrations by imaging a number of objects of known geometry at different orientations.

## Supplementary Information

OpenDrop is freely available at `http://opencolloids.com`.

## Acknowledgments

This work was supported in part by the Australian Research Council through a Discovery Project Grant (DP140100677). MJN acknowledges funding from the David Hay Postgraduate Award. The Particulate Fluids Processing Centre, University of Melbourne is thanked for infrastructure support. We are indebted to the many students who have patiently assisted with beta-testing the software in the course of their experiments.

## Appendix A. Fletcher's criteria for setting $\lambda$

The Levenberg–Marquardt–Fletcher algorithm updates the parameter set $\boldsymbol{\beta}$ according to

$$\boldsymbol{\beta}^{(k+1)} = \boldsymbol{\beta}^{(k)} + \boldsymbol{\delta} \tag{A.1}$$

where $\boldsymbol{\delta}$ is determined by solving

$$\left(\mathbf{J}^{\mathrm{T}}\mathbf{J} + \lambda \operatorname{diag}(\mathbf{J}^{\mathrm{T}}\mathbf{J})\right)\boldsymbol{\delta} = -\mathbf{J}^{\mathrm{T}}\boldsymbol{e}. \tag{A.2}$$

In this Appendix we outline the criteria outlined by Fletcher [28] for setting $\lambda$. From Eq. (A.2), when $\lambda = 0$ this routine reduces to Gauss–Newton, while as $\lambda \to \infty$ the parameters are updated in a step parallel to steepest descent. This method essentially interpolates between these two routines based on the value of $\lambda$.

In his method, Fletcher introduced the ratio $R$ of the actual reduction in the objective $S - S'$ ($S$ is the previous objective function, $S'$ is the new objective function) to the predicted reduction if the system was converging quadratically as predicted by Gauss–Newton,

$$R = \frac{S - S'}{-2\boldsymbol{\delta}^{\mathrm{T}}\boldsymbol{v} - \boldsymbol{\delta}^{\mathrm{T}}\mathbf{A}\boldsymbol{\delta}} \tag{A.3}$$

where $\mathbf{A} = \mathbf{J}^{\mathrm{T}}\mathbf{J}$ and $\boldsymbol{v} = \mathbf{J}^{\mathrm{T}}\boldsymbol{e}$. This ratio quantifies the rate of convergence for the algorithm. By comparing this rate to two predetermined values $\rho$ and $\sigma$ (with $0 < \rho < \sigma < 1$, Fletcher suggests taking $\rho = 0.25$ and $\sigma = 0.75$), it is possible to determine if the convergence is rapid, $R > \sigma$, or poor, $R < \rho$. If the convergence is rapid ($R > \sigma$), the value of $\lambda$ is reduced by a factor of 2, while if the convergence is poor ($R < \rho$), the value of $\lambda$ is increased by a factor $\nu$. For intermediate convergence rates ($\rho \leqslant R \leqslant \sigma$), the value of $\lambda$ is left unchanged.

For the case where the convergence is poor ($R < \sigma$), $\lambda$ is determined by minimising a quadratic interpolation of the objective function $S$ in the direction of $\alpha\boldsymbol{\delta}$. Minimising this interpolation leads to the optimal step size

$$\alpha = \frac{1}{2 - (S' - S)/(\boldsymbol{\delta}^{\mathrm{T}}\boldsymbol{v})}. \tag{A.4}$$

From this the multiple $\nu \equiv 1/\alpha$ is determined which is used to update $\lambda$. This multiple is replaced by 2 or 10 if it is less than 2 or greater than 10, respectively.

In addition, Fletcher introduction a 'cut-off' value $\lambda_c$, below which $\lambda$ is set to zero, thus allowing the algorithm to adopt the complete Gauss–Newton algorithm. Fletcher provides a theoretical justification for the choice of $\lambda_c$ to be the reciprocal of the smallest eigenvalue of $\mathbf{A}^{-1}$. As this is computationally expensive, he underestimates this

$$\lambda_c = \frac{1}{\|\mathbf{A}^{-1}\|_\infty} \equiv \frac{1}{\max|\mathbf{A}^{-1}|}. \tag{A.5}$$

and only calculates this when $\lambda$ is increased from zero. The complete Levenberg–Marquardt–Fletcher algorithm is illustrated in Fig. 9.

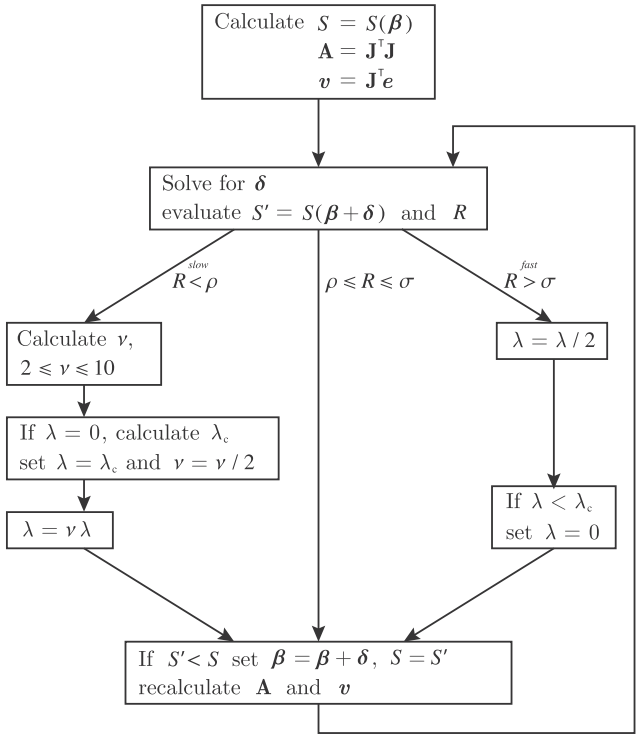


**Fig. 9.** Flow chart for the Levenberg–Marquardt–Fletcher algorithm. When $R > \sigma$, convergence is rapid resulting in a smaller value of $\lambda$, biasing the system towards the Gauss–Newton algorithm, whereas for poor convergence, $R < \rho$, the value of $\lambda$ is increased, thereby biasing the system towards steepest descent. Adapted from Fletcher [28].

## Appendix B. The residual vector and Jacobian matrix

We proceed by deriving expressions for the residual vector and the Jacobian matrix, before discussing an iterative procedure for calculating the arc lengths $\bar{s}_i$ in the next section. The residual vector has elements $\boldsymbol{e}_i = e_i$ where

$$e_i^2 = e_i^r(\bar{s}_i)^2 + e_i^z(\bar{s}_i)^2 \tag{B.1}$$

where we have introduced the arc length $\bar{s}_i$ which corresponds to the closest theoretical point to the $i$th data point. By trigonometry:

$$\begin{aligned} e_i^r(\bar{s}) &= |(x_i - X_0)\cos\omega - (y_i - Y_0)\sin\omega| - R_0\bar{r}(\bar{s}) \\ &= \pm\{(x_i - X_0)\cos\omega - (y_i - Y_0)\sin\omega\} - R_0\bar{r}(\bar{s}) \end{aligned} \tag{B.2a}$$

$$e_i^z(\bar{s}) = ((x_i - X_0)\sin\omega + (y_i - Y_0)\cos\omega) - R_0\bar{z}(\bar{s}). \tag{B.2b}$$

The Jacobian matrix can be determined by applying the chain rule to Eq. (B.1);

$$\mathbf{J}_{ij} = \frac{\partial e_i}{\partial \beta_j} = \frac{1}{2e_i}\frac{\partial}{\partial \beta_j}(e_i^2) \tag{B.3}$$

$$= \frac{1}{\sqrt{e_i^r(\bar{s}_i)^2 + e_i^z(\bar{s}_i)^2}}\left(e_i^r(\bar{s}_i)\left.\frac{\partial e_i^r}{\partial \beta_j}\right|_{\bar{s}_i} + e_i^z(\bar{s}_i)\left.\frac{\partial e_i^z}{\partial \beta_j}\right|_{\bar{s}_i}\right). \tag{B.4}$$

We now calculate the derivatives $\partial e_i^r/\partial\beta_j$ and $\partial e_i^z/\partial\beta_j$ by differentiating Eq. (B.2) with respect to each of the parameters in $\boldsymbol{\beta} = \{X_0, Y_0, \omega, R_0, \mathrm{Bo}\}$:

$$\frac{\partial e_i^r}{\partial X_0} = \mp\cos\omega \qquad \frac{\partial e_i^z}{\partial X_0} = -\sin\omega \tag{B.5a}$$

$$\frac{\partial e_i^r}{\partial Y_0} = \pm\sin\omega \qquad \frac{\partial e_i^z}{\partial Y_0} = -\cos\omega \tag{B.5b}$$

$$\begin{aligned} \frac{\partial e_i^r}{\partial \omega} &= \mp((x_i - X_0)\sin\omega + (y_i - Y_0)\cos\omega) \\ \frac{\partial e_i^z}{\partial \omega} &= ((x_i - X_0)\cos\omega - (y_i - Y_0)\sin\omega) \end{aligned} \tag{B.5c}$$

$$\frac{\partial e_i^r}{\partial R_0} = -\bar{r}(\bar{s}_i) \qquad \frac{\partial e_i^z}{\partial R_0} = -\bar{z}(\bar{s}_i) \tag{B.5d}$$

$$\frac{\partial e_i^r}{\partial \mathrm{Bo}} = -R_0\frac{\partial \bar{r}}{\partial \mathrm{Bo}} \qquad \frac{\partial e_i^z}{\partial \mathrm{Bo}} = -R_0\frac{\partial \bar{z}}{\partial \mathrm{Bo}} \tag{B.5e}$$

where the ambiguous signs in Eq. (B.5), are taken to match the choice of sign in Eq. (B.2a). Each of these partial derivatives are known explicitly, except for the partial derivatives with respect to the Bond number in Eq. (B.5e), which arise due to the implicit dependence the functions $\bar{r}$ and $\bar{z}$ have on the Bond number from Eq. (2)

$$\bar{r}(\bar{s}) \equiv \bar{r}(\bar{s};\mathrm{Bo}), \quad \bar{z}(\bar{s}) \equiv \bar{z}(\bar{s};\mathrm{Bo}). \tag{B.6}$$

The partial derivatives with respect to the Bond number must therefore be determined by solving a set of coupled differential equations, formed by differentiating Eq. (2) with respect to the Bond number Bo, and then interchanging the order of differentiation. This leads to a set of coupled partial differential equations. For constant Bo, these derivatives can be integrated numerically as a set of coupled ordinary differential equations

$$\frac{\mathrm{d}}{\mathrm{d}\bar{s}}\left(\left.\frac{\partial\varphi}{\partial\mathrm{Bo}}\right|_{\mathrm{Bo}}\right) + -\bar{z} - \left.\frac{\partial\bar{z}}{\partial\mathrm{Bo}}\right|_{\mathrm{Bo}}\mathrm{Bo} - \left.\frac{\partial\varphi}{\partial\mathrm{Bo}}\right|_{\mathrm{Bo}}\frac{\cos\varphi}{\bar{r}} + \left.\frac{\partial\bar{r}}{\partial\mathrm{Bo}}\right|_{\mathrm{Bo}}\frac{\sin\varphi}{\bar{r}^2} \tag{B.7a}$$

$$\frac{\mathrm{d}}{\mathrm{d}\bar{s}}\left(\left.\frac{\partial\bar{r}}{\partial\mathrm{Bo}}\right|_{\mathrm{Bo}}\right) + -\left.\frac{\partial\varphi}{\partial\mathrm{Bo}}\right|_{\mathrm{Bo}}\sin\varphi \tag{B.7b}$$

$$\frac{\mathrm{d}}{\mathrm{d}\bar{s}}\left(\left.\frac{\partial\bar{z}}{\partial\mathrm{Bo}}\right|_{\mathrm{Bo}}\right) + \left.\frac{\partial\varphi}{\partial\mathrm{Bo}}\right|_{\mathrm{Bo}}\cos\varphi \tag{B.7c}$$

where the associated boundary conditions are determined by differentiating the boundary conditions in Eq. (4), leading to

$$\left.\frac{\partial\varphi}{\partial\mathrm{Bo}}\right|_{\mathrm{Bo}} = 0, \quad \left.\frac{\partial\bar{r}}{\partial\mathrm{Bo}}\right|_{\mathrm{Bo}} = 0, \quad \left.\frac{\partial\bar{z}}{\partial\mathrm{Bo}}\right|_{\mathrm{Bo}} = 0 \quad \text{at} \quad \bar{s} = 0. \tag{B.8}$$

## Appendix C. Calculating the arc lengths

We now outline the method used to calculate the arc length $\bar{s}_i$ that minimise the associated Euclidean distance between the $i$th data point and the theoretical drop profile, enabling the residual vector and the Jacobian matrix to be determined from Eq. (B.1) and (B.4).

The arc length $\bar{s}_i$ is the arc length for which the Euclidean distance between the $i$th data point and the theoretical curve is minimised

$$e_i^2 \equiv e_i^r(\bar{s}_i)^2 + e_i^z(\bar{s}_i)^2 \equiv \min_{\bar{s}}\left\{e_i^r(\bar{s})^2 + e_i^z(\bar{s})^2\right\}. \tag{C.1}$$

Introducing the function $f_i(\bar{s})$ which is the derivative of the distance between the $i$th data point and the theoretical drop profile, we can find $\bar{s}_i$ by finding the root of $f_i(\bar{s})$. To perform this procedure we implement a Newton–Raphson routine, which iteratively updates $\bar{s}_i^{(k)}$ according to

$$\bar{s}_i^{(k+1)} = \bar{s}_i^{(k)} - \frac{f_i(\bar{s}_i^{(k)})}{f_i'(\bar{s}_i^{(k)})} \equiv \bar{s}_i^{(k)} - g_i(\bar{s}_i^{(k)}). \tag{C.2}$$

This iteration is repeated until the arc length converges to within a specified tolerance, *i.e.* $|\,\bar{s}_i^{(k+1)} - \bar{s}_i^{(k)}\,| \equiv |\,g_i(\bar{s}_i^{(k)})\,| <$ tol. Through differentiation the required functions can be found

$$f_i(\bar{s}) \equiv \frac{\mathrm{d}}{\mathrm{d}\bar{s}}\left(e_i^r(\bar{s})^2 + e_i^z(\bar{s})^2\right) = -2R_0\left(e_i^r(\bar{s})\cos\varphi(\bar{s}) + e_i^z(\bar{s})\sin\varphi(\bar{s})\right) \tag{C.3}$$

and

$$f_i'(\bar{s}) = 2R_0\left\{R_0 + \frac{\mathrm{d}\varphi}{\mathrm{d}\bar{s}}\left(e_i^r(\bar{s})\sin\varphi(\bar{s}) - e_i^z(\bar{s})\cos\varphi(\bar{s})\right)\right\}. \tag{C.4}$$

Combining Eq. (C.3) and (C.4) leads to an expression for $g_i(\bar{s})$, defined in Eq. (C.2),

$$g_i(\bar{s}) = -\frac{e_i^r(\bar{s})\cos\varphi(\bar{s}) + e_i^z(\bar{s})\sin\varphi(\bar{s})}{R_0 + \frac{\mathrm{d}\varphi}{\mathrm{d}\bar{s}}(\bar{s})\left\{e_i^r(\bar{s})\sin\varphi(\bar{s}) - e_i^z(\bar{s})\cos\varphi(\bar{s})\right\}}. \tag{C.5}$$

## References


[1] J. Eggers, Rev. Mod. Phys. 69 (3) (1997) 865–929.
[2] J. Eggers, E. Villermaux, Physics of liquid jets, Rep. Prog. Phys. 71 (2008) 036601.
[3] J. Drelich, C. Fang, C.L. White, Measurement of interfacial tension in fluid–fluid systems, Encyclopedia of Surface and Colloid Science, second ed., vol. 4, CRC Press, Boca Raton, 2006. Ch.
[4] A.M. Worthington, Proc. R. Soc. Lond. 32 (1881) 362–377.
[5] A.M. Worthington, Philos. Mag. 19 (5) (1885) 46–48.
[6] A. Ferguson, Philos. Mag. 23 (6) (1911) 417–430.
[7] F. Bashforth, J.C. Adams, An Attempt to Test the Theories of Capillary Action: By Comparing the Theoretical and Measured Forms of Drops of Fluid, University Press, 1883.
[8] T.Z. Harmathy, AIChE J. 6 (2) (1960) 281–288.
[9] A. Merrington, E. Richardson, Proc. Phys. Soc. 59 (1) (1947) 1–13.
[10] W. Bond, D.A. Newton, Lond. Edin. Dublin Philos. Mag. J. Sci. Ser. 7 5 (30) (1928) 794–800.
[11] J.M. Andreas, E.A. Hauser, W.B. Tucker, J. Phys. Chem. 42 (8) (1938) 1001–1019.
[12] S. Fordham, Proc. R. Soc. Lond. A 194 (1036) (1948) 1–16.
[13] D. Niederhauser, F. Bartell, Annual report of progress–fundamental research on occurrence and recovery of petroleum 1948–1949, American Petroleum Institute, Baltimore, 1949–1950.
[14] Y. Rotenberg, L. Boruvka, A.W. Neumann, J. Colloid Interface Sci. 93 (1) (1983) 169–183.
[15] C. Huh, R.L. Reed, J. Colloid Interface Sci. 91 (2) (1983) 472–484.
[16] M. Hoorfar, A.W. Neumann, Adv. Colloid Interface Sci. 121 (1) (2006) 25–49.
[17] J.W. Jennings, N.R. Pallas, Langmuir 4 (4) (1988) 959–967.
[18] K. Levenberg, Q. Appl. Math. 2 (1944) 164–168.
[19] D.W. Marquardt, J. Soc. Ind. Appl. Math. 11 (2) (1963) 431–441.
[20] O.I. del Río, A.W. Neumann, J. Colloid Interface Sci. 196 (2) (1997) 136–147.
[21] N.J. Alvarez, L.M. Walker, S.L. Anna, J. Colloid Interface Sci. 333 (2) (2009) 557–562.
[22] N.M. Dingle, K. Tjiptowidjojo, O.A. Basaran, M.T. Harris, J. Colloid Interface Sci. 286 (2005) 647–660.
[23] C. Ferrera, J. Montanero, M. Cabezas, Meas. Sci. Technol. 18 (12) (2007) 3713–-3723.
[24] E. Vega, J. Montanero, M. Herrada, C. Ferrera, Phys. Rev. E 90 (1) (2014) 013015.
[25] A. Kalantarian, R. David, J. Chen, A.W. Neumann, Langmuir 27 (7) (2011) 3485–3495.
[26] M.J. Neeson, D.Y.C. Chan, R.F. Tabor, Langmuir 30 (51) (2014) 15388–15391.
[27] J. Canny, IEEE Trans. Pattern Anal. (6) (1986) 679–698.
[28] R. Fletcher, A modified marquardt subroutine for non-linear squares, Tech. rep., Atomic Energy Research Establishment, Harwell (England), 1971.
[29] N.B. Vargaftik, B.N. Volkov, L.D. Voljak, J. Phys. Chem. Ref. Data 12 (1983) 817–820.
[30] R.C. Weast (Ed.), CRC Handbook of Chemistry and Physics, fifteenth ed., The Chemical Rubber Co., Boca Raton, 1969.
[31] A.S. Kabalnov, K.N. Makarov, O.V. Shchereakova, J. Fluorine Chem. 50 (1990) 271–284.
[32] Z. Adamczyk, G. Para, P. Warszynski, Langmuir 15 (1999) 8383–8387.
[33] J.J. Jasper, J. Phys. Chem. Ref. Data 1 (1972) 841–1009.
[34] J.C. Berg (Ed.), An Introduction to Interfaces and Colloids, World Scientific, Singapore, 2010.
[35] A. Czajka, G. Hazell, J. Eastoe, Surfactants at the Design Limit, Langmuir. http://dx.doi.org/10.1021/acs.langmuir.5b00336.
[36] Y.-M. Tricot, Surfactants: static and dynamic surface tension, Liquid Film Coating, Springer, Amsterdam, 1997. Ch.
[37] V.B. Fainerman, R. Miller, The maximum bubble pressure technique, Drops and Bubbles in Interfacial Research, Elsevier, Amsterdam, 1998. Ch.
[38] W.D.E. Thomas, L. Potter, J. Colloid Interface Sci. 50 (1975) 397–412.
[39] R. Picknett, R. Bexon, J. Colloid Interface Sci. 61 (2) (1977) 336–350.
[40] M.J. Neeson, R.R. Dagastine, D.Y.C. Chan, R.F. Tabor, Soft Matter 10 (2014) 8489–8499.
[41] T. Tate, Philos. Mag. 27 (1864) 176–180.
[42] W.D. Harkins, F.E. Brown, J. Am. Chem. Soc. 41 (1919) 499–524.
[43] J.P. Garandet, B. Vinet, P. Gros, J. Colloid Interface Sci. 165 (1994) 351–354.
[44] R. Myrvold, F.K. Hansen, J. Colloid Interface Sci. 207 (1998) 97–105.
[45] L.G. Cascão Pereira, O. Théodoly, H.W. Blanch, C.J. Radke, Langmuir 19 (2003) 2349–2356.
[46] S.S. Dukhin, G. Kretzschmar, R. Miller (Eds.), Dynamics of Adsorption at Liquid Interfaces, Elsevier, Amsterdam, 1995.
[47] R. Miller, Z. Policova, R. Sedev, A.W. Neumann, Colloids Surf. A 76 (1993) 179–185.
[48] A. Yeung, T. Dabros, J. Masliyah, Langmuir 13 (1997) 6597–6606.
[49] A. Yeung, L. Zhang, Langmuir 22 (2006) 693–701.
[50] J. Kim, L.J. Cote, F. Kim, W. Yuan, K.R. Shull, J. Huang, J. Am. Chem. Soc. 132 (2010) 8180–8186.
[51] J.D. Berry, M.R. Davidson, D.J.E. Harvie, J. Comput. Phys. 251 (2013) 209–222.
[52] R.F. Tabor, F. Grieser, R.R. Dagastine, D.Y.C. Chan, J. Colloid Interface Sci. 371 (2012) 1–14.
[53] M.H.W. Hendrix, R. Manica, E. Klaseboer, D.Y.C. Chan, C.-D. Ohl, Phys. Rev. Lett. 108 (2012) 247803.